



Multiple beam ptychography for large field-of-view, high throughput, quantitative phase contrast imaging



Charles Bevis*, Robert Karl Jr, Jonathan Reichenadter, Dennis F. Gardner, Christina Porter, Elisabeth Shanblatt, Michael Tanksalvala, Giulia F. Mancini, Henry Kapteyn, Margaret Murnane, Daniel Adams

JILA, University of Colorado, 440 UCB, Boulder, Colorado 80309-0440, USA

ARTICLE INFO

Article history:

Received 2 November 2016

Revised 25 July 2017

Accepted 29 August 2017

Available online 6 September 2017

Keywords:

Ptychography

Coherent diffractive imaging

Phase retrieval

ABSTRACT

The ability to record large field-of-view images without a loss in spatial resolution is of crucial importance for imaging science. For most imaging techniques however, an increase in field-of-view comes at the cost of decreased resolution. Here we present a novel extension to ptychographic coherent diffractive imaging that permits simultaneous full-field imaging of multiple locations by illuminating the sample with spatially separated, interfering probes. This technique allows for large field-of-view imaging in amplitude and phase while maintaining diffraction-limited resolution, without an increase in collected data i.e. diffraction patterns acquired.

© 2017 Elsevier B.V. All rights reserved.

1. Introduction

Ptychography coherent diffractive imaging (CDI) is a phase-contrast imaging technique capable of providing quantitative, high fidelity reconstructions of the complex amplitude of an object of interest [1–3]. Unlike conventional CDI [4], ptychography CDI introduces translational diversity into data acquisition by scanning an illuminating probe across an extended object and recording the diffracted light at many positions, each with an overlapping field-of-view. The redundancy in the data over-constrains the phase retrieval problem, allowing a unique complex transmission or reflection function for the object to be recovered, depending on the imaging mode used [5,6]. Moreover, the redundancy in a ptychographic data set can also be used to recover the complex amplitude of the illumination beam [1,3], correct for experimental errors in scan positions [7–9], solve for missing diffraction data [10], perform super-resolution imaging [11], and deconvolve the incoherent modes of the illuminating function and mode-specific response of an object [12,13].

Another significant accomplishment of ptychography CDI is its ability to mitigate the Nyquist sampling condition on the diffracted wave intensity that previously limited the sample size when using single-diffraction-pattern CDI techniques [14]. To overcome this constraint, ptychography CDI generally operates in an area-by-area

scanning modality, allowing for an image field-of-view that grows with the size of a scan. This comes at the cost of increased scan time and data acquisition required. Indeed, the limited throughput of ptychographic imaging systems remains an obstacle for large field-of-view imaging.

Previous work that made progress on this challenge includes the implementation of a single-shot ptychographic experimental configuration [15] that is capable of producing images with near diffraction-limited spatial resolution when used with visible light. However, because of its reliance on refractive optics, it is difficult to implement in regions of the spectrum (e.g. X-ray) where quality optics are simply not available. An alternative sampling criteria [16,17] has been proposed which frees a ptychographic imaging system from the oversampling criteria common to other CDI techniques, allowing a larger illuminating probe to be used during a scan. However, systems using this sampling criterion do not efficiently scale to large field-of-view images due to an increased redundancy in the overlap of adjacent scan positions. Thus, a practical implementation allowing for a diffraction-limited, large field-of-view ptychographic imaging system is yet to be realized. Recent work has shown that by spatially separating the modes of the illuminating beam or by using multiple *mutually incoherent* illuminating beams, multimode ptychography algorithms [12,13] can be used to reconstruct a larger field-of-view without an increase in data acquisition or loss in resolution [18].

In this work, we demonstrate diffraction-limited, large field-of-view ptychographic imaging using multiple, spatially separated, *mutually coherent* illuminating probes. This increases the

* Corresponding author.

E-mail address: charles.bevis@colorado.edu (C. Bevis).

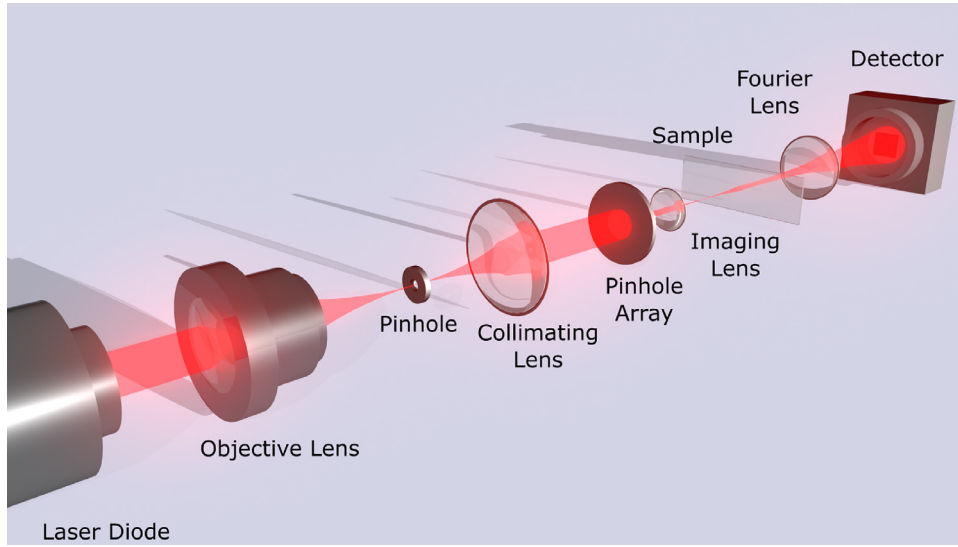


Fig. 1. The experimental geometry for this proof-of-principle demonstration. Note the exact specifications of the pinhole array is dependent on the type of filtering technique implemented in the apparatus.

throughput of the microscope by a factor corresponding to the number of probes, while leaving the scan time and acquired data volume unchanged. When configured for optimal performance, this technique represents the most efficient use of the ptychographic data set for large field-of-view imaging to date. Using an optical transmission mode CDI microscope as shown in Fig. 1, we explore large field-of-view imaging capabilities using three unique methods to image three different samples. Finally, we discuss the image fidelity of the reconstructed objects and compare images obtained using both multi-beam and single-beam ptychography imaging modalities.

2. Methods

In ptychography CDI, the illuminating probe is subject to an oversampling constraint [19,20] that restricts its transverse size. Satisfying the oversampling constraint allows the resulting diffraction intensities to be Nyquist sampled by the detector. However, if a second illuminating probe is added to the system, interference terms between the two probes will be introduced at the detector. Traditional ptychography algorithms interpret these two individual probes as a single illumination function, which greatly restricts the allowable size and separation of the probes on the sample, as the entire probe system must satisfy the oversampling condition.

It is possible to suppress this interference and effectively convert the measured signal to an incoherent sum of the diffraction from all the probes. This suppression can be achieved through digital filtering of the data after acquisition, which we refer to as *autocorrelation filtering* (Section 2.1). In a complementary approach, the experimental parameters can be tuned to naturally remove the interference from the measured signal, which we refer to as *alias cloaking* (Section 2.2).

2.1. Autocorrelation filtering

Consider a transmission ptychography experiment with two identical, mutually coherent, beams with finite support incident on an extended sample, and separated by a center-to-center distance $\Delta\mathbf{x}$ and wavelength λ . We work in the projection approximation such that the full exit surface wave just after the sample is given by the sum of the contributions from each probe function multiplied by the object i.e.: $\psi(\mathbf{x}) = O(\mathbf{x})P_1(\mathbf{x}) + O(\mathbf{x})P_2(\mathbf{x} - \Delta\mathbf{x})$, where

$\psi(\mathbf{x})$ is the exit surface wave, $O(\mathbf{x})$ is the object transmission function, and $P_n(\mathbf{x})$ is the n^{th} probe function. During a scan, a detector positioned in the far-field a distance z away, will record the intensity of the diffracted wave as

$$I(\mathbf{f}) = |\mathcal{F}\{\psi(\mathbf{x})\}|^2, \quad (1)$$

where $\mathcal{F}\{\}$ is the 2D Fourier transform operator. Using the form of $\psi(\mathbf{x})$ given above, we compute the Fourier transform. Using the convention $\tilde{H}(\mathbf{f}) \equiv \mathcal{F}\{H(\mathbf{x})\}$:

$$\begin{aligned} \mathcal{F}\{\psi(\mathbf{x})\} &= \mathcal{F}\{O(\mathbf{x})P_1(\mathbf{x}) + O(\mathbf{x})P_2(\mathbf{x} - \Delta\mathbf{x})\} \\ &= \tilde{O}(\mathbf{f}) \otimes \tilde{P}_1(\mathbf{f}) + \tilde{O}(\mathbf{f}) \otimes [\tilde{P}_2(\mathbf{f})e^{2\pi i(\Delta\mathbf{x} \cdot \mathbf{f})}]. \end{aligned} \quad (2)$$

Where \otimes is the 2D convolution operator. Taking the absolute square gives the intensity of the wave at the detector, I^{det} .

$$\begin{aligned} I^{\text{det}}(\mathbf{f}) &= |\tilde{O}(\mathbf{f}) \otimes \tilde{P}_1(\mathbf{f}) + \tilde{O}(\mathbf{f}) \otimes [\tilde{P}_2(\mathbf{f})e^{2\pi i(\Delta\mathbf{x} \cdot \mathbf{f})}]|^2 \\ &= |\tilde{O}(\mathbf{f}) \otimes \tilde{P}_1(\mathbf{f})|^2 + |\tilde{O}(\mathbf{f}) \otimes [\tilde{P}_2(\mathbf{f})e^{2\pi i(\Delta\mathbf{x} \cdot \mathbf{f})}]|^2 \\ &\quad + (\tilde{O}(\mathbf{f}) \otimes \tilde{P}_1(\mathbf{f}))(\tilde{O}(\mathbf{f}) \otimes [\tilde{P}_2(\mathbf{f})e^{2\pi i(\Delta\mathbf{x} \cdot \mathbf{f})}])^* \\ &\quad + (\tilde{O}(\mathbf{f}) \otimes \tilde{P}_1(\mathbf{f}))^*(\tilde{O}(\mathbf{f}) \otimes [\tilde{P}_2(\mathbf{f})e^{2\pi i(\Delta\mathbf{x} \cdot \mathbf{f})}]), \end{aligned} \quad (3)$$

where $()^*$ indicates the complex conjugate of the quantities enclosed. Here, we clearly see that in addition to a sum of the intensity of the diffracted waves, we also have a cross term that gives rise to interference on the detector. Multimode ptychography algorithms are not designed to interpret interference arising from multiple coherent probes. So before such algorithms are employed, this interference must be removed.

By examining the functional form of the convolution operation, the following term can be rewritten

$$\tilde{O}(\mathbf{f}) \otimes [\tilde{P}_2(\mathbf{f})e^{2\pi i(\Delta\mathbf{x} \cdot \mathbf{f})}] = e^{-2\pi i(\Delta\mathbf{x} \cdot \mathbf{f})}(\tilde{O}(\mathbf{f})e^{2\pi i(\Delta\mathbf{x} \cdot \mathbf{f})} \otimes \tilde{P}_2(\mathbf{f})) \quad (4)$$

Eq. (3) is now rewritten as

$$\begin{aligned} I^{\text{det}}(\mathbf{f}) &= |\tilde{O}(\mathbf{f}) \otimes \tilde{P}_1(\mathbf{f})|^2 + |[\tilde{O}(\mathbf{f})e^{2\pi i(\Delta\mathbf{x} \cdot \mathbf{f})}] \otimes \tilde{P}_2(\mathbf{f})|^2 \\ &\quad + (\tilde{O}(\mathbf{f}) \otimes \tilde{P}_1(\mathbf{f}))([\tilde{O}(\mathbf{f})e^{2\pi i(\Delta\mathbf{x} \cdot \mathbf{f})}] \otimes \tilde{P}_2(\mathbf{f}))^* e^{2\pi i(\Delta\mathbf{x} \cdot \mathbf{f})} \\ &\quad + (\tilde{O}(\mathbf{f}) \otimes \tilde{P}_1(\mathbf{f}))^*([\tilde{O}(\mathbf{f})e^{2\pi i(\Delta\mathbf{x} \cdot \mathbf{f})}] \otimes \tilde{P}_2(\mathbf{f}))e^{-2\pi i(\Delta\mathbf{x} \cdot \mathbf{f})}. \end{aligned} \quad (5)$$

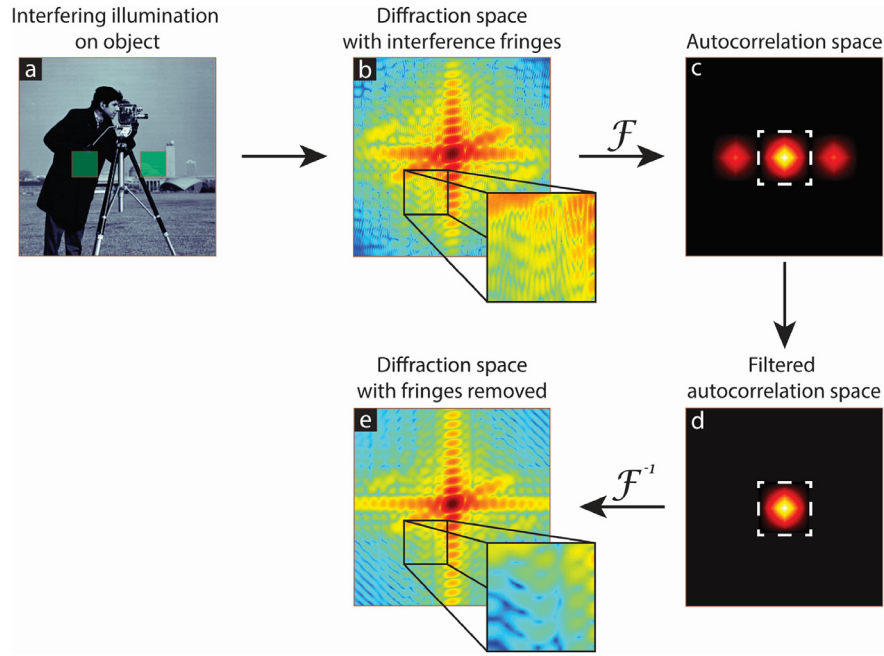


Fig. 2. A flowchart depicting the process of autocorrelation filtering. (a) Two coherent probes (green squares) are incident on an object. (b) The resulting field propagates to a detector located in the far field, recording a diffraction pattern that contains interference from the interaction of the exit surface wave of each probe. (c) Fourier transforming the signal intensity brings it into autocorrelation space, where the (d) incoherent sum of the exit surface waves (central peak) can be filtered from the interference terms (side peaks), provided the system satisfies Eq. (7). (e) Inverse transforming the filtered signal yields an incoherent sum of the diffraction from each probe that can then be used for the reconstruction. (For interpretation of the references to color in this figure legend, the reader is referred to the web version of this article.)

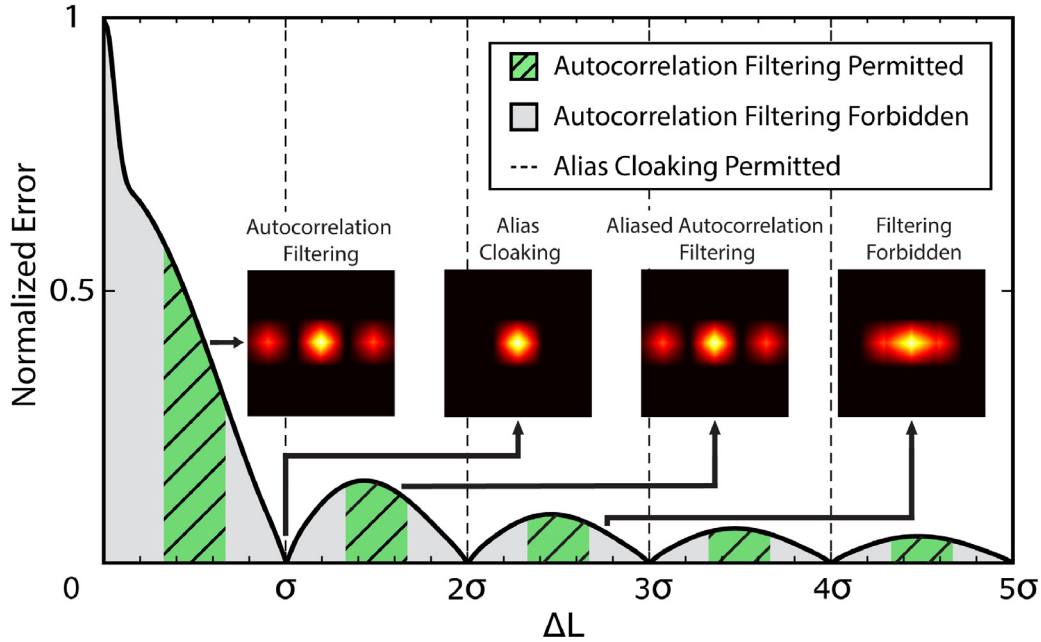


Fig. 3. The results of a simulation showing the dependence of the normalized error introduced by the presence of interference fringes on the signal as a function of the dimensionless parameter $\Delta L = \Delta x/D$. The exact form of this curve depends on the shape of the probe functions. This simulation was performed using two square illuminating probes, with an oversampling for each individual probe of $\sigma = 6$. The multiple regions where autocorrelation filtering is permitted are shown in striped green regions while the local minima indicate points where alias cloaking is permitted. The width of these regions will also vary with σ , in accordance with Eq. (7). The smaller insets depict autocorrelation space as it appears in the various filtering regions. (For interpretation of the references to color in this figure legend, the reader is referred to the web version of this article.)

Now, in a procedure similar to [21], we take the Fourier transform of the intensity given in Eq. (5) which brings us to the autocorrelation space of the diffracted surface wave. Eq. (5) then becomes

$$\mathcal{F}\{I^{det}(\mathbf{f})\} = O(\mathbf{x})P_1(\mathbf{x}) \star O(\mathbf{x})P_1(\mathbf{x}) + O(\mathbf{x} - \Delta\mathbf{x})P_2(\mathbf{x}) \star O(\mathbf{x} - \Delta\mathbf{x})P_2(\mathbf{x})$$

$$+ [O(\mathbf{x})P_1(\mathbf{x}) \star O(\mathbf{x} - \Delta\mathbf{x})P_2(\mathbf{x})]^* \otimes \delta(\mathbf{x} + \Delta\mathbf{x}) + [O(\mathbf{x})P_1(\mathbf{x}) \star O(\mathbf{x} - \Delta\mathbf{x})P_2(\mathbf{x})] \otimes \delta(\mathbf{x} - \Delta\mathbf{x}), \quad (6)$$

with \star representing a 2D cross-correlation. The first two terms in Eq. (6) contain information pertaining to the autocorrelation of each term of the exit surface wave $\psi(\mathbf{x})$. The last two terms can be thought of as the cross-correlation of the contributions to $\psi(\mathbf{x})$

from the two probes and contain the information regarding the interference at the detector plane. Notice, each cross-correlation term is shifted by an amount $\pm \Delta \mathbf{x}$ due to the shifting property of the Dirac delta distribution. Because the probe functions have finite support, each term in Eq. (6) is also of finite extent, with a width equal to the sum of each individual probe. This results in distinct autocorrelation and cross-correlation “peaks” when viewing the data in this space.

With careful selection of diameter and separation of the illuminating beams, it is possible to isolate the autocorrelation terms from the cross-correlation terms. Then, by applying a filter to remove the cross-correlation peaks and inverse transforming, the interference is removed and we are left with data composed of the incoherent sum of the diffraction produced from each term in $\psi(\mathbf{x})$. The filtered data can then be used with an incoherent multimode ptychography algorithm to reconstruct a complex image of both the illuminated fields-of-view of the object and the incident probe functions. This process is represented in Fig. 2, where the autocorrelation and cross-correlation peaks are seen to be distinct in autocorrelation space.

As long as the cross-correlation and autocorrelation peaks do not overlap in autocorrelation space, this filtering is possible. We can use this requirement to define regions of the parameter space where filtering is permitted. First, we consider that the cross-correlation peaks must be sufficiently offset from the central autocorrelation peaks such that there is no spatial overlap between them. This means the separation between the probes, $\Delta \mathbf{x}$, must be larger than the full width of the central autocorrelation peak. The autocorrelation of a function with finite support is twice the width of the function itself. Defining the characteristic probe width in the object plane, D , we find the lower bound for the probe separation to be $\Delta \mathbf{x} \geq 2D$.

We define the linear oversampling of a single beam as $\sigma = \lambda z / p D$, where λ is the central wavelength of light, z is the distance from the object plane to detector plane, and p is the detector pixel size. Using relations between the detector and object plane, we define $\mathbb{X} \equiv \lambda z / p$ as the reconstructed field-of-view per scan position. With this new definition, the oversampling may be written as $\sigma = \mathbb{X}/D$. Most CDI techniques require $\sigma \geq 2$ [14].

When autocorrelation filtering, we must also consider the additional information present in our data that must be removed through filtering. This means the system must provide room for each peak in autocorrelation space to exist without overlapping with the central peak, which places the additional constraint that central autocorrelation peak should be no larger than half the field-of-view of the reconstructed object, or in terms of the oversampling parameter: $\sigma \geq 4$. Considering the geometry that leads to the most efficient packing of information in autocorrelation space, such that the various cross-correlation peaks are just shy of intersecting with the central maximum, the upper bound for the probe separation is $\Delta \mathbf{x} \leq \mathbb{X} - 2D$.

As the probe separation increases, the frequency of the interference fringes also increases, until they become greater than the sampling frequency of the detector and begins to alias. Severe aliasing causes the cross-correlation peaks to cyclically shift toward and away from the autocorrelation peak, giving rise to many regions where autocorrelation filtering is possible. These conditions are best expressed in the dimensionless inequality

$$2 \leq \text{mod}\left(\frac{\Delta \mathbf{x}}{D}, \sigma\right) \leq \sigma - 2 \quad (7)$$

where mod is the modulus operator.

To examine the performance of this filtering technique, we consider the deviations of the interfering signal intensity, S_I , to that of a signal intensity produced by a single probe function, S_N . We compare these deviations as a function of a

dimensionless parameter $\Delta L \equiv \Delta \mathbf{x}/D$. We characterize this deviation using a root-mean-square error metric of the form: $\varepsilon_{rms}(\Delta L) = \sqrt{\frac{1}{M} \sum_m [S_I(\Delta L) - S_N(\Delta L)]^2}$, where M is the number of elements within each signal. We then normalize this error by the RMS value of S_N to arrive at a normalized error that characterizes the relative impact of the interference fringes as a function of probe separation and individual probe size. Fig. 3 shows the result of a simulation depicting the dependence of the normalized error as ΔL is varied. Here, multiple regions where autocorrelation filtering is permitted are swept through, in accordance with Eq. (7). The allowed regions are shown in green with diagonal black striping. Thus, greater experimental flexibility is realized as we see there are repeating regions of parameter space where this autocorrelation filtering technique is valid.

2.2. Alias cloaking

Referring again to Fig. 3, we see that as ΔL is varied, there are points where the error introduced by the interference fringes is naturally minimized. In the previous section we showed that it was necessary to couple our beam separation with the oversampling of a single beam in the system, forcing a limitation on an individual probe size such that $\sigma \geq 4$. This allows Eq. (7) to be satisfied and the various cross-correlation and autocorrelation peaks remain distinct in autocorrelation space. The typical requirement in CDI is $\sigma \geq 2$, so autocorrelation filtering does not allow the largest possible probe size permitted by the system.

In order to overcome this limitation, we construct a system where the cross-correlation peaks are suppressed without the need for digital filtering, as is automatically the case when probes of non-interfering modes are used [12,13,18]. In terms of autocorrelation space, this allows the central peak to fill the entire space, maximizing the allowable size of the input beam and the information collected per scan position. This is accomplished by shifting the filtering process from a post-processing technique to an experimental condition in which we take advantage of aliasing effects due to the finite pixel size of the detector.

To begin, we rewrite Eq. (5), so that the intensity on the detector is written as

$$I^{det}(\mathbf{f}) = |\tilde{O}(\mathbf{f}) \otimes \tilde{P}_1(\mathbf{f})|^2 + |[\tilde{O}(\mathbf{f})e^{2\pi i(\Delta \mathbf{x} \cdot \mathbf{f})}] \otimes \tilde{P}_2(\mathbf{f})|^2 + 2|\tilde{O}(\mathbf{f}) \otimes \tilde{P}_1(\mathbf{f})| |\tilde{O}(\mathbf{f})e^{2\pi i(\Delta \mathbf{x} \cdot \mathbf{f})}] \otimes \tilde{P}_2(\mathbf{f})| \cos[2\pi i(\Delta \mathbf{x} \cdot \mathbf{f})]. \quad (8)$$

Written in this form, and using the mapping between frequency and detector space, $\mathbf{f} = \mathbf{x}/\lambda z$, it becomes obvious the inference between the two beams on the detector occurs with some mean frequency given by $f_I = \Delta \mathbf{x}/\lambda z$, with $\Delta \mathbf{x} = |\Delta \mathbf{x}|$. The signal is sampled at the detector with a frequency $f_s = 1/p$. However, because the pixels are finite, the value recorded by the detector is the integrated intensity within the pixel area. We now take f_I to be greater than f_s , such that the detector under samples f_I . In this scenario, the interference frequency is aliased back to some frequency given by

$$f_a = \text{mod}(f_I, f_s). \quad (9)$$

The interference frequency is aliased to zero when f_I is an integer multiple of f_s . By equating f_I and f_s , we find this aliasing occurs at the critical probe separation

$$\Delta x_c = \frac{N\lambda z}{p}, \quad (10)$$

where N is an integer.

Due to the finite size of the detector pixels, the visibility of the interference at frequencies in the vicinity of f_I are also suppressed.

Thus, by tuning the separation of the probes, it is possible to suppress the frequencies contributing to the interference fringes, making the cross term in Eq. (8) small in comparison to the incoherent sum term. It is true that only one frequency is completely suppressed using this method, though frequencies in the vicinity of f_i are also attenuated. These frequencies are treated in detail in the Supplemental Information. Once aliased, the recorded data effectively appear to be an incoherent sum of the diffraction data from each individual probe and can be directly reconstructed using a multimode ptychography algorithm.

As the ratio of $\Delta x/D$ becomes larger, the slope of the error surrounding the minima decreases, meaning the system becomes more resilient to misalignment as the beam separation is increased. Fig. 3 can be further extended to show that at large values of ΔL , the error introduced by the interference is naturally suppressed at all values of Δx thus the restrictions on the system parameters to obtain alias cloaking are greatly relaxed.

3. Experimental results

The schematic of our visible-wavelength transmission-mode ptychographic microscope is shown in Fig. 1. Although the two methods described above require a slightly different apparatus, they share common elements to produce and shape the beam, as described here. We use a fiber-coupled laser diode, [Blue Sky Research FTEC2 658–60, $\lambda = 656$ nm] which propagates through a spatial filter [Newport, 900: with a $5\mu\text{m}$ pinhole 900PH-5 and M-10X objective]. The filtered beam is then collimated by a lens with focal length $f = 5$ cm. At this point the setup must be optimized for the different techniques and samples, as described for each experiment below.

3.1. Autocorrelation filtering

Using the setup described above, a collimated beam is transmitted through a pinhole mask consisting of three pinholes in an L-shape formation, fabricated using black aluminum foil [Thorlabs, BKF12] in which three holes are punched. The pinholes ranged in size from $90\text{--}175\mu\text{m}$, with separations of approximately 0.75 mm. The pinholes are imaged onto the sample using an imaging lens with focal length $f = 10$ cm; the imaging system has magnification $M = 1$. The incident light is scattered through a Negative United States Air Force (NUSAF) resolution test chart [Thorlabs, R3L3S1N] and is captured by a Fourier transform lens with focal length $f = 2$ cm, which focuses the scattered light onto a Mightex [SCN-B013-U] CMOS detector. A schematic of the experiment is shown in Fig. 4(a). Given these system parameters, we calculate the oversampling of each individual beam to range from $10\text{--}15$, with the parameter ΔL falling between $7.8\text{--}11.8$, satisfying Eq. (7) without any aliasing in the signal.

Data were recorded at 121 scan positions in an 11×11 rectangular grid with random offsets of 20% to avoid periodic artifacts [22]. At each position, multiple exposures were captured with exposure times ranging from 0.05 ms to 750 ms. The resulting images were combined, increasing the dynamic range of the detector from 68 dB to 100 dB [23]. Before applying autocorrelation filtering, we first attempted to reconstruct the entire probe system using the ePIE algorithm [3]. However, doing so forces the algorithm to treat the multiple probes as a single system, which, because of the large separation between the two probes, the exit surface wave is not properly sampled on the detector and the reconstruction failed to produce a meaningful reconstruction. We next treated these data using the using the filtering technique described in Section 2.1, where the autocorrelation of each scatter pattern was computed and filtered to remove the interference between the

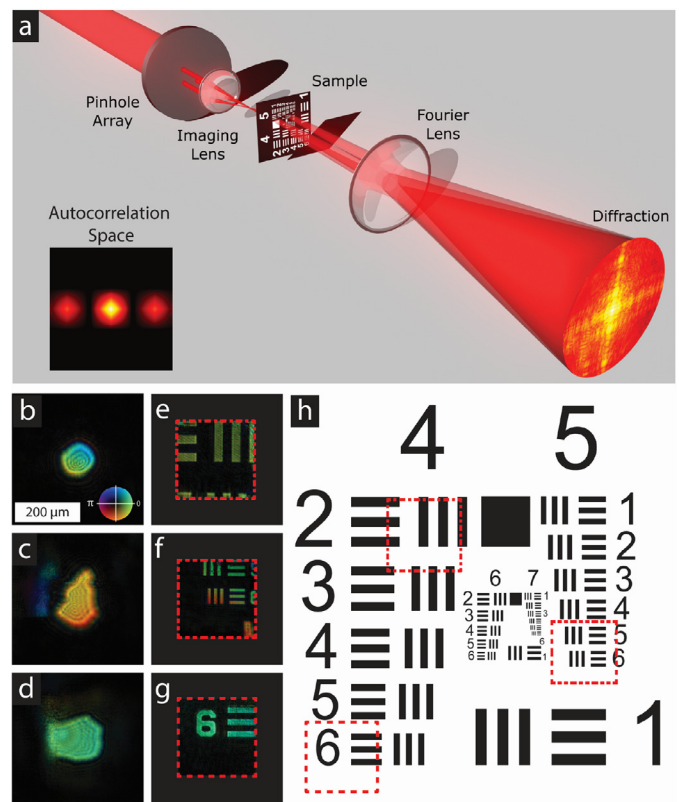


Fig. 4. (a) The experimental setup used to test the autocorrelation filtering technique, the small inset displays an example of autocorrelation space for the pinhole array used during this experiment. (b–c) The complex amplitude of the reconstructed probes recovered from the multimode ptychographic reconstruction after autocorrelation filtering, brightness is amplitude and hue represents phase. (e–f) The complex amplitude of the reconstructed image of the NUSAF test chart sample. (h) A diagram of groups 4–7 of a USAF resolution test chart. The dashed lines show the relative positions of each reconstructed area in (e–f). The recovered probes and objects are paired by row. The scale bar of $200\mu\text{m}$ and color wheel shown in (b) are common for (c–g). (For interpretation of the references to color in this figure legend, the reader is referred to the web version of this article.)

multiple probes. A modified version of the multimode ptychography algorithm described in [13] was used to reconstruct the complex valued object and probe for each beam. Fig. 4 displays the amplitude of the three reconstructed probe functions (b–d) and the reconstructed amplitudes of the imaged NUSAF resolution test chart (e–g). The asymmetric shaped probe functions recovered by the algorithm are a result of the inexact method used to fabricate the pinhole mask.

To further study the capabilities of autocorrelation filtering, we adjusted the microscope such that the frequency of interference between our beams would alias on the detector and then performed a similar analysis. A new pinhole mask was fabricated, consisting of two circular pinholes, each with $D = 0.4$ mm in diameter, separated by a distance of $\Delta x = 3.7$ mm. Due to the large probe separations in this experiment, the transform lens was replaced with an aspherical lens [Thorlabs AL2520-B] of equivalent parameters to reduce the spherical aberrations on the recorded diffraction data. Given the other system parameters, we calculated an individual beam oversampling $\sigma = 6.3$ and $\Delta L = 9.3$. Referring to Fig. 3, these parameters place the system in the second allowable filtering region, meaning the signal interference has aliased to a lower frequency. The imaging system was removed in favor of placing the pinhole mask in close proximity to the sample to simplify the experimental setup. To test the versatility of the system, we exchanged the NUSAF resolution test chart for a sample consisting of

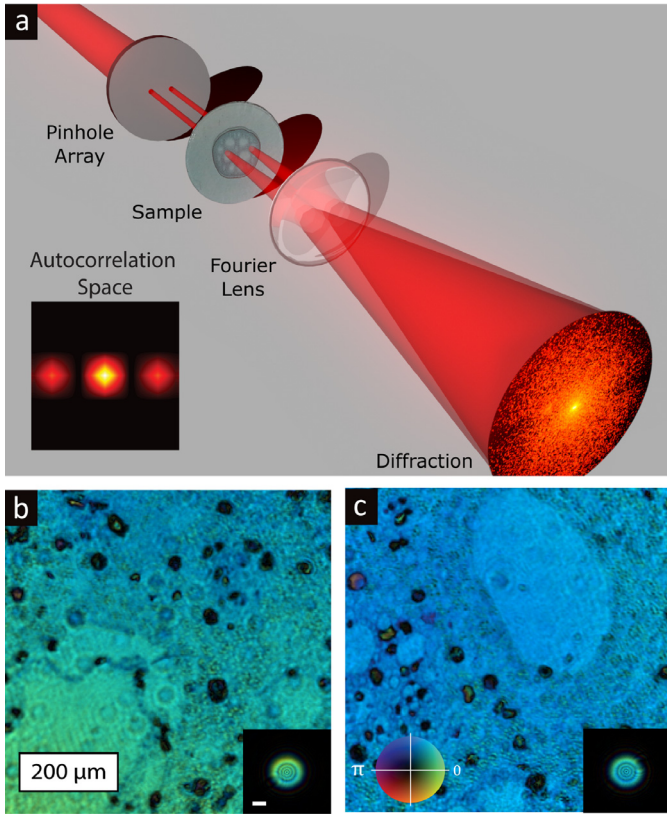


Fig. 5. The experimental schematic for aliased autocorrelation filtering, the small inset displays an example of autocorrelation space for the pinhole array used during this experiment. (b–c) The reconstructed complex amplitudes of the nymphaea of aquistio sample and the illuminating probes. The scale bars represent 200 μm in the object field-of-view and probe inset field-of-view respectively. The scale bars and color scheme are equivalent for both b and c. In these images brightness indicates the amplitude and hue corresponds to phase.

a nymphaea of aquistio stem mounted on a microscope slide and preserved in cedar wood oil [Amscope PS25]. The modified experiment is shown in Fig. 5(a), the distances are exaggerated for schematic clarity.

A 64-position ptychography scan was recorded arranged in an 8×8 rectilinear grid, with 20% random offsets between adjacent scan positions. Data were processed identically to the previous experiment, where autocorrelation filtering was applied to remove the interference terms and reconstructed using a multimode ptychography algorithm [13]. The reconstructed amplitudes of each object and probe are shown in Fig. 5(b–c).

3.2. Alias cloaking

To demonstrate the capabilities of a ptychography microscope with alias cloaking implemented, we engineered a system in such a way that the individual probe diameter is the maximum size allowable for conventional ptychography CDI, corresponding to an oversampling of $\sigma = 2$. The pinhole mask consists of three circular apertures arranged in a linear pattern, each with a diameter $D = 1.26 \text{ mm}$ and probe-to-probe separation of $\Delta x = 2.5 \text{ mm}$. The three identical beams were incident on a sample consisting of cells from a thin transverse slice of a rabbit testicle mounted on a microscope slide and preserved in cedar wood oil [AmScope PS25]. Fig. 6(d) shows the schematic of this system. With these system parameters, Eq. (10) is satisfied with $N = 1$, placing this experimental configuration in the first minima of Fig. 3, appropriate for alias cloaking.

We recorded a ptychography scan consisting of 784 scan positions arranged in a 28×28 grid with a step size of $D/12$ modulated with a 20% random offset. The large number of scan positions, coupled with the scan position step size and beam diameter, yield overlapping fields of view in the reconstructed objects. Because the diffraction-limited resolution of each reconstruction is independent of the collective probe system, each object retains a high spatial resolution. The three object reconstructions were combined into a single, large field-of-view, high-resolution image, shown in Fig. 6(a). The total reconstructed area is 21.5 mm^2 . Fig. 6(b) shows an enlarged region given by the black square outline in Fig. 6(a).

After reconstruction, we found a quadratic phase present in all three reconstructed objects used to create Fig. 6(a). The phase was persistent across the object reconstructions and is indicative of the sample being slightly curved. To verify the presence of this result, we placed the sample in an interferometer [Zygo GPI XP] to independently measure the sample curvature. The Zygo measurements confirmed the second order phase on the sample. For viewing purposes, this quadratic phase was removed from Fig. 6(a,b). The phase oscillations present in Fig. 6(a) are due to a misalignment during data acquisition that left a strong back reflection on the detector, offset from the central DC component of the recorded diffraction data. The separation between the back reflection and the DC component of each scatter pattern and relative angle are consistent with the angle and period seen in the oscillations in Fig. 6(a). In principle, these oscillations can be removed either by blocking the back scatter or with a modification to the algorithm used for reconstruction where the affected region of the scatter pattern is not used.

We also note that we attempted to reconstruct this data set using the ePIE algorithm. In this case, the algorithm was able to converge to a solution, however, the object and probe reconstruction obtained was a superposition of the three mutually coherent probes with a vastly decreased image fidelity when compared to the results obtained using the treatment described above.

4. Image analysis

Previous work using multimode ptychography algorithms has shown that the process of multiplexing data has no noticeable effect on the reconstructed resolution of the complex amplitude of the object function [13]. For completeness, we investigate the effect that coherent filtering has on the system. We compare the resolution of equivalent regions of the sample in the multiple beam reconstruction shown in Fig. 6(a) and a reconstruction obtained from a single beam ptychography scan. We define the phase retrieval transfer function (PRTF) [6,24,25] computed as

$$\text{PRTF}(f_r) = \left\langle \frac{\left| \sum_n \langle \psi_n^{\text{rec}}(\mathbf{x}_j) \rangle_i \right|}{\sqrt{\langle I^{\text{meas}}(\mathbf{x}_j) \rangle_j}} \right\rangle_\varphi \quad (11)$$

where $\psi_n^{\text{rec}}(\mathbf{x}_j)$ is the j^{th} reconstructed diffraction pattern generated by the n^{th} probe and $I^{\text{meas}}(\mathbf{x}_j)$ is the intensity measurement corresponding to the j^{th} scan position. $\langle \rangle_i$ and $\langle \rangle_j$ represent an average over i independent reconstructions and the j scan positions, while $\langle \rangle_\varphi$ indicates an azimuthal average over annuli of constant numerical aperture, with a width of four pixels. For the data presented in this work, the PRTF was computed by averaging the results of 100 independent ptychography reconstructions, each of which ran for 500 iterations, at which point the retrieved image was considered converged.

An estimate for the resolution is found by locating the spatial frequency corresponding to the point where the PRTF falls below 0.5 [25]. This cutoff frequency gives an estimated spatial resolution of $2.85 \mu\text{m}$ for the alias cloaking reconstruction and $2.70 \mu\text{m}$

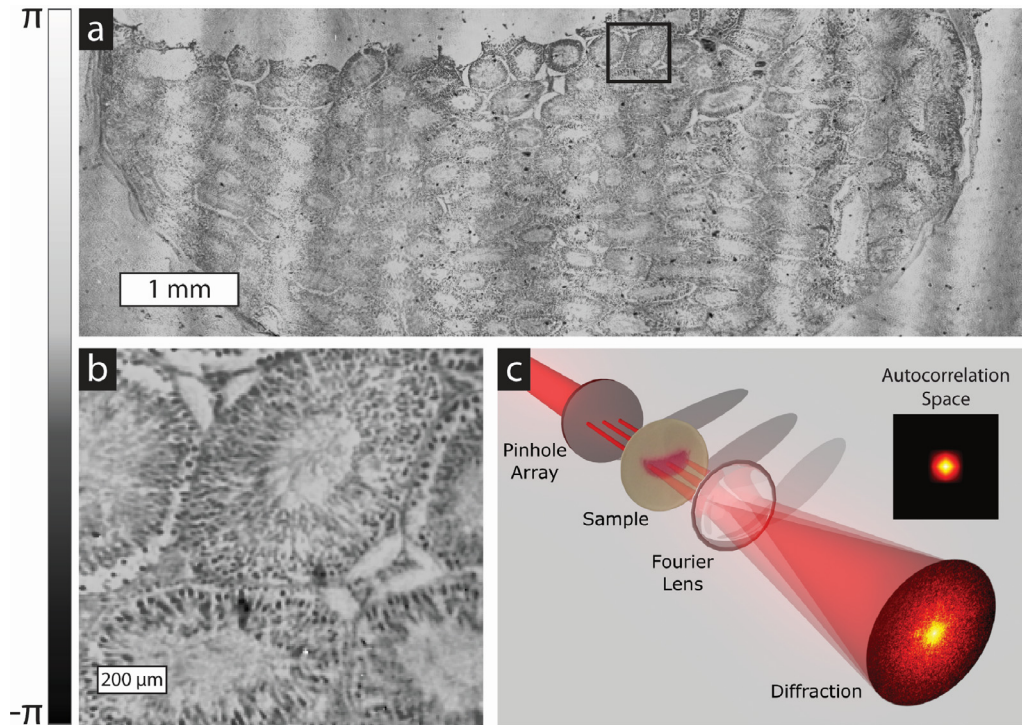


Fig. 6. (a) Large FOV phase reconstruction of a cross-sectional slice of a rabbit testicle obtained using alias cloaking ptychography. (a) is composed of reconstructed objects from three identical beams simultaneously incident on the sample, each imaging one third of the specimen. (b) An enhanced region shown by the black square outline in (a). (c) Experimental apparatus used to obtain the reconstructions shown in (a, b), where the small inset displays an example of autocorrelation space for the pinhole array used during this experiment. Notice the cross-correlation peaks are naturally suppressed. Scale bars are 1 mm (a) and 100 μm (b).

for the single beam scan. The Abbe diffraction-limited resolution the microscope is calculated to be $2.48 \mu\text{m}$. In addition, we compare the azimuthally averaged power spectral density (PSD) of a subset of the reconstructed object in Fig. 6(a) with an equivalent field-of-view reconstruction from a single beam scan. The PSD for each reconstruction is shown in Fig. 7(a) while the areas used to calculate the PSD are shown in Fig. 7(c,d). The ratio between the PSD is displayed in Fig. 7(b) and has an average value of 0.98, with deviation strongly attributed to the low spatial frequency components. This deviation is attributed to the back reflection present in the data set used to obtain Figs. 6(a) and 7(c).

The results of the PRTF and PSD analysis indicate that there is no noticeable loss in resolution in the reconstructed objects when the alias cloaking technique is used. We note, however, that the maximum number of allowable beams is limited by the dynamic range of the detector as in multiplexed holography [26]. The exact relation between reconstruction quality and detector dynamic range is left as a subject for future study.

Care must also be taken when configuring an experimental system to ensure that the number of beams used is supported by the multimode algorithm. Though we are not aware of an in-depth study of this behavior, we can apply simple arguments from information theory to this problem where a comparison is made between the amount of information to be solved for (i.e. the pixel values for the reconstructed objects and probes) and the amount of information collected via the intensity data for each scatter pattern. In multimode ptychography, as the number of modes is increased, so is the number of unknowns in the system. Thus, for a given set of parameters, it could be possible to construct a system that is not solvable by these arguments. However, provided the stability the experiment is sufficient, this issue can be overcome by increasing the number of positions within a scan, collecting more information and thus increasing the number of knowns vs. unknowns in the system.

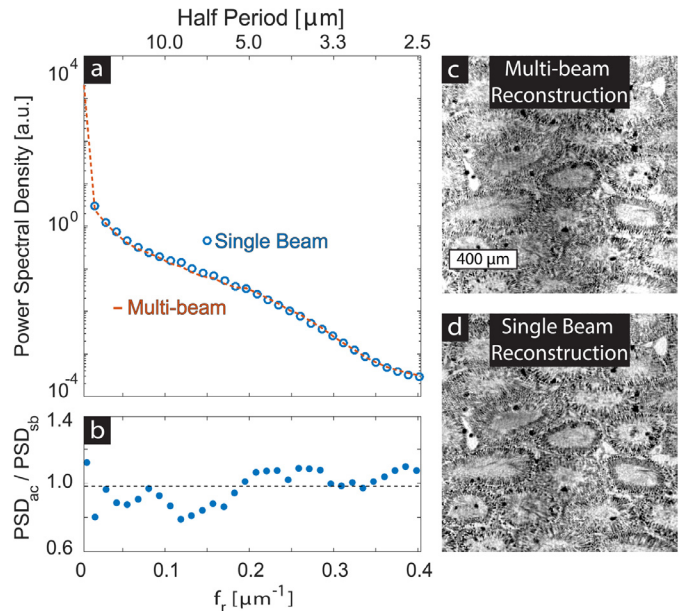


Fig. 7. (a) The azimuthally averaged power spectral density of two phase map reconstructions. One obtained while using an alias cloaking experimental geometry (c) and one obtained using conventional single beam ptychography (d). The field-of-view and scales are equivalent in (c–d). (b) displays the ratio of the power spectral density shown in (a) a function of spatial frequency. The mean value of this ratio is 0.98. The similarity of the PSD for the two different imaging modalities indicates that the two imaging techniques produce similar results.

5. Discussion and conclusions

The throughput of a ptychographic imaging system is a key factor that limits the applicability of this powerful imaging

technique. The diffraction-limited, high-throughput imaging with inherent phase contrast obtained with CDI imaging techniques is of great interest in the field of bio-imaging and material characterization, where large scale properties are inherently linked to the behavior and characterization of local order, interactions, and phenomena. In this work, we provided a proof-of-principle demonstration of two novel techniques allowing the use of multiple coherent illuminating probes to simultaneously image multiple areas of a sample. These techniques provide a method for removing the interference between the coherent probes, allowing the data to be processed using a multimode ptychography algorithm.

Multiple beam ptychography provides large field-of-view, high-throughput imaging while minimizing the required data acquisition. This imaging technique is implemented by controlling the relative placement of the illuminating probes and can be applied in either data post-processing through autocorrelation filtering, or experimentally through alias cloaking. We showed high fidelity reconstructions when samples were simultaneously illuminated by either two or three coherent probe beams. This technique can be extended to use many simultaneous illuminating functions, the upper limit of which is the subject for future studies. We expect this technique to find application in the X-ray and EUV spectral ranges, where large field-of-view images with nanometer spatial resolution can provide key insight into the relationship between microscopic order and macroscopic material properties.

Acknowledgments

This work was supported by the DARPA PULSE program, an NSF MRSEC grant [DMR-1420620](#), and the NSF STC on Real-Time Functional Imaging (STROBE) grant [DMR-1548924](#). C.B., D.G., and C.P. acknowledge support from the NSF GRFP. R.K. acknowledges support from an NDSEG fellowship.

References

- [1] P. Thibault, M. Dierolf, A. Menzel, O. Bunk, C. David, F. Pfeiffer, High-resolution scanning x-ray diffraction microscopy, *Science* 321 (5887) (2008) 379–382.
- [2] J.M. Rodenburg, et al., Hard-x-ray lensless imaging of extended objects, *Phys. Rev. Lett.* 98 (3) (2007) 34801.
- [3] A.M. Maiden, J.M. Rodenburg, An improved ptychographical phase retrieval algorithm for diffractive imaging, *Ultramicroscopy* 109 (10) (2009) 1256–1262.
- [4] J.R. Fienup, Phase retrieval algorithms: a comparison, *Appl. Opt.* 21 (15) (1982) 2758–2769.
- [5] M.D. Seaberg, et al., Tabletop nanometer extreme ultraviolet imaging in an extended reflection mode using coherent Fresnel ptychography: supplementary material, *Optica* 1 (1) (2014) 39.
- [6] B. Zhang, et al., High contrast 3D imaging of surfaces near the wavelength limit using tabletop EUV ptychography, *Ultramicroscopy* 158 (2015) 98–104.
- [7] A.M. Maiden, M.J. Humphry, M.C. Sarahan, B. Kraus, J.M. Rodenburg, An annealing algorithm to correct positioning errors in ptychography, *Ultramicroscopy* 120 (2012) 64–72.
- [8] F. Zhang, et al., Translation position determination in ptychographic coherent diffraction imaging, *Opt. Express* 21 (11) (2013) 13592–13606.
- [9] M. Guizar-Sicairos, J.R. Fienup, Phase retrieval with transverse translation diversity: a nonlinear optimization approach, *Opt. Express* 16 (10) (2008) 7264–7278.
- [10] H. Liu, Z. Xu, X. Zhang, Y. Wu, Z. Guo, R. Tai, Effects of missing low-frequency information on ptychographic and plane-wave coherent diffraction imaging, *Appl. Opt.* 52 (11) (2013) 2416–2427.
- [11] A.M. Maiden, M.J. Humphry, F. Zhang, J.M. Rodenburg, Superresolution imaging via ptychography, *J. Opt. Soc. Am. A. Opt. Image Sci. Vis.* 28 (4) (2011) 604–612.
- [12] P. Thibault, A. Menzel, Reconstructing state mixtures from diffraction measurements, *Nature* 494 (7435) (2013) 68–71.
- [13] D.J. Batey, D. Claus, J.M. Rodenburg, Information multiplexing in ptychography, *Ultramicroscopy* 138C (2013) 13–21.
- [14] J.C.H. Spence, U. Weierstall, M. Howells, Coherence and sampling requirements for diffractive imaging, *Ultramicroscopy* 101 (2–4) (2004) 149–152.
- [15] P. Sidorenko, O. Cohen, Single-shot ptychography, *Optica* 3 (1) (2016) 9.
- [16] T.B. Edo, et al., Sampling in x-ray ptychography, *Phys. Rev. A* 87 (5) (2013) 53850.
- [17] D.J. Batey, et al., Reciprocal-space up-sampling from real-space oversampling in x-ray ptychography, *Phys. Rev. A* 89 (4) (2014) 43812.
- [18] R. Karl, et al., Spatial, spectral, and polarization multiplexed ptychography, *Opt. Express* 23 (23) (2015) 30250.
- [19] R.H.T. Bates, Fourier phase problems are uniquely solvable in more than one dimension. I: underlying theory, *Optik (Stuttg)* 61 (3) (1982) 247–262.
- [20] J. Miao, D. Sayre, H. Chapman, Phase retrieval from the magnitude of the Fourier transforms of nonperiodic objects, *JOSA A* 15 (6) (1998) 1662–1669.
- [21] B. Leshem, et al., Direct single-shot phase retrieval from the diffraction pattern of separated objects, *Nat. Commun.* 7 (2016) 10820.
- [22] M. Dierolf, et al., Ptychographic coherent diffractive imaging of weakly scattering specimens, *New J. Phys.* 12 (2010).
- [23] M.A. Robertson, R.L. Stevenson, Estimation-theoretic approach to dynamic range enhancement using multiple exposures, *J. Electron. Imaging* 12 (2003) 219–228.
- [24] R.N. Wilke, et al., Hard X-ray imaging of bacterial cells: nano-diffraction and ptychographic reconstruction, *Opt. Express* 20 (17) (2012) 19232.
- [25] J.A. Rodriguez, et al., Three-dimensional coherent X-ray diffractive imaging of whole frozen-hydrated cells, *IUCr* 2 (5) (2015) 575–583.
- [26] J.A. Dominguez-Caballero, N. Loomis, G. Barbastathis, J. Milgram, Techniques based on digital multiplexing holography for three-dimensional object tracking, in: *Lasers Electro-Optics, 2007. CLEO 2007. Conf., 2007*, pp. 1–2.